

A phase-space-compressing, mass-selecting beamline for hyperthermal, focused ion beam deposition

Kevin J. Boyd, Adam Łapicki, Masato Aizawa, and Scott L. Anderson

Department of Chemistry, University of Utah, 315 South 1400 East RM Dock, Salt Lake City, Utah 84112-0850

(Received 14 April 1998; accepted for publication 8 September 1998)

We have developed an ion beamline for hyperthermal ion-surface collisions that incorporates a phase-space compressor to improve the focusability/current density of the ion beam in the 1–10 eV deposition energy range. In essence, collisional damping is used to substantially improve the brightness of the ion source. In addition to the focusing behavior, the beamline also accomplishes mass selection, source-target pressure reduction of $> 10^{10}$, confinement of the beam to avoid space charge spreading, and hyperthermal energy beam transport. For our application the requirement is moderately tight (100 s of microns) focusing at hyperthermal energies (1–100 eV), but the principle should also be applicable to improving spot sizes/current densities at higher energies. © 1998 American Institute of Physics. [S0034-6748(98)01512-3]

I. INTRODUCTION

We have constructed an experiment designed to allow deposition of mass-selected ions on well characterized surfaces in ultrahigh vacuum (UHV). This instrument is being used to study chemistry at cluster–solid interfaces, hyperthermal energy subplantation, and can be applied to catalytic chemistry as well. In the process, we have developed an ion deposition beamline with some novel features that should be of interest in other ion/surface scattering and focused ion beam applications.

Some cluster-surface experiments require that we deposit cluster ions at energies low enough to avoid damaging the substrate and/or completely disrupting the clusters upon impact. For clusters of a few to a few tens of atoms, deposition energies down to a few electron volts are desirable. For other experiments, deposition energies up to a few hundred electron volts are required. The major difficulty with mass-selected cluster ion deposition is the rather low intensities of available cluster ion sources (e.g., 10^6 to 10^7 /s per size). Surface analysis tools that provide chemical insight, such as x-ray photoelectron spectroscopy or electron energy loss spectrometry, are rather insensitive, requiring on the order of 10^{13} to 10^{14} deposited atoms/cm². The combination of low intensity and low sensitivity makes it difficult to deposit usable samples in a time short enough to avoid surface contamination from adsorption of background gases, even in UHV.

The same problems affect any ion deposition experiment, although it is easier to scale-up the ion beam intensity for stable atomic and molecular ions. Even in these systems, achieving mass-selected ion deposition rates large enough for film growth is nontrivial, particularly at low or hyperthermal deposition energies.¹

One approach to the sensitivity problem is to increase the output from the cluster source, and this has been done successfully for small clusters by several groups.^{2–12} For large clusters (100–1000 s atoms/cluster), controlling growth

conditions in a gas-aggregation source can yield clusters in a narrow size range,^{13–23} but this approach is not applicable to the smaller sizes of interest to us. It is also possible to study the deposited clusters with more sensitive surface analysis tools, such as scanning probe microscopy,^{24,25} however, much of the chemical information is lost.

One feature of surface analysis tools that partly offsets their low sensitivities is the ability to analyze small spots. Since intensity is inversely proportional to the focal radius squared, shrinking the deposited spot can lead to dramatic intensity improvements. The ultimate limit to the focusability of an ion beam is determined by Liouville's theorem.²⁶ This well-known theorem states that the phase-space volume of the ion beam, i.e., the product of the spatial and momentum distributions, is conserved in the absence of dissipative forces. Most cluster sources tend to produce large diameter beams, sometimes with large momentum distributions as well; i.e., large phase-space volumes. Conversely, producing a focused beam at hyperthermal energies requires narrow spatial and momentum distributions, i.e., a small phase space volume. One goal of our beamline design is, therefore, to reduce the phase space volume of our beam.

For a continuous beam, beam quality is usually discussed²⁷ in terms of the absolute emittance, ϵ , rather than phase space volume. ϵ is defined as the product of the extents of the spatial and divergence angle distributions of the beam. The *normalized* emittance, ϵ_n , is defined as $\epsilon_n = \beta \times \gamma \times \epsilon$, where β is v/c , v is the beam velocity, and γ is $(1 - \beta^2)^{-1/2}$. For our nonrelativistic beam $\gamma = 1$, and $\epsilon_n = \epsilon \times v/c$. A result of the Liouville theorem is that ϵ_n is constant in the absence of dissipative forces, and thus the absolute emittance is inversely proportional to v . Because focusability is determined by the absolute emittance, the most common approach to reducing focal spot size is simply to increase the beam energy. This approach is not useful for our purposes, however, because we wish to deposit at the lowest possible energies. Small spots at hyperthermal energies re-

quire an actual reduction in the total phase space volume or normalized emittance.

To reduce the phase space volume, it is necessary to introduce a damping force. Damping for hyperthermal energy ions can be accomplished by allowing collisions with a thermal buffer gas, preventing beam spreading by confining the ions in some sort of trap. Gerlich and co-workers have used this approach for many years in a storage ion source where ions are created, then thermalized in a multipole radio-frequency (rf) trap.^{28,29} We have used a similar approach to collect and thermalize metal cluster ions produced in external sputter and laser ablation sources, generating beams for gas-phase scattering experiments.^{30–47} More recently, Gerlich and co-workers have used a cryogenic rf trap to cool and study subthermal energy collisions of ions from an external source.^{48,49}

In the experiments just mentioned, the trap geometry was optimized for cooling the translational and internal energies of the ions. For this purpose, sharply inhomogeneous rf fields are required, and high-order multipole (>20 pole) geometries were used. Because these traps have large, nearly field-free central volumes, there is little reduction in the spatial size of the ion beam/cloud. It is possible to simultaneously compress both spatial and momentum distributions by using a low order multipole, and this technique is routinely used in quadrupole ion trap mass spectrometers to improve trapping of injected ion pulses. Leisner *et al.*⁵⁰ have used gas collisions during passage through a linear quadrupole to dampen the considerable kinetic energy distribution of their sputtered ion beam, allowing soft landing in a matrix. The quadrupole trap system described below uses a “bottle” geometry to lengthen trapping times, improving the collisional cooling for our continuous ion beam. In addition, the geometry increases the radial compression of the beam, allowing us to couple a relatively large ion source to a small diameter, hyperthermal energy beam transport system.

There are other practical problems associated with deposition in UHV. The ion sources can operate at pressure up to tens of mbar, thus we need to maintain a source-to-target pressure differential of at least ten orders of magnitude. We also need to mass select the cluster ion beam and want to be able to use a variable width mass bandpass. This rules out conventional magnetic sector or Wien mass filters, since they are spatially dispersive, and thus degrade the phase-space distribution.

In the absence of a confining potential, space-charge repulsion limits beam size and current density. Freeman⁵¹ has shown that these effects are proportional to $j \times m^{1/2} \times E^{-3/2}$, where j is the current density, m the ion mass, and E the beam kinetic energy. High current density thus demands high ion transport energy, particularly for high mass ions. Previous low-energy ion deposition beamlines have consequently been of the “accel-decel” type, where ions are accelerated to higher energies (>1 kV) for transport through the beamline, then decelerated just before deposition.^{52–60} Space charge in these beamlines is partially compensated by low energy electrons obtained from ion collisions with background gas or chamber walls. This leads to additional problems, however. Ion-electron recombination can produce high

energy neutrals, and to avoid substrate damage, these must be removed from the beam prior to deceleration onto the target.¹ In addition, the electron-ion equilibrium needed to suppress space-charge effects must be reestablished after every change in field, for example, after mass selectors, neutral dumps, etc. Along with the other features mentioned, the beamline described below uses rf ion trapping/guiding methods to transport and confine the beam, allowing ion transport at hyperthermal energies while preventing space charge-driven expansion of the beam diameter.

II. EXPERIMENTAL DESIGN

We first give an overview of the instrument, followed by construction details for the beamline components, followed by a discussion of the operating principles with some illustrative results.

A. Overview

A schematic of the instrument is shown in Fig. 1. Ions can be produced by a variety of methods, ranging from simple electron impact for atomic and molecular ions, to magnetron sputtering/gas aggregation for large clusters. The ions are collected by the compressing quadrupole ion trap, where phase-space compression by storage in helium or argon occurs. The beam from the compressing quadrupole is focused into the low-pass quadrupole guide (“quad”) by an einzel lens that also serves as a differential pumping aperture. The low-pass quad transports the ions and serves as a low-pass mass filter, rejecting ions with mass/charge (m/Q) greater than an adjustable cutoff value. This quad passes through two bulkheads, allowing three stages of differential pumping along its length. At the end of the low-pass quad, the ions pass through a four element lens/differential pumping aperture into the high-pass quad. So that we can service the beamline and source without venting the UHV section of the instrument, a miniature pneumatically operated gate valve is built into this lens system. The high-pass quad transports the beam to the focusing lens system, and also serves to reject ions with m/Q less than an adjustable cutoff value. The combination of the low- and high-pass filters serves as the desired variable-bandpass mass filter. The total length of the beamline, source-to-target is ~ 2.5 m. The length is partly to allow better mass discrimination in the quads, and partly to improve differential pumping by reducing the intensity of the rare gas beam effusing from the compressing quad chamber.

At the exit of the final quad, the ions are accelerated and focused by a set of five disk-shaped lenses. The final lens also serves as an exposure mask, defining the maximum size of the beam deposited on the substrate. For the initial experiments described below, a cylindrical mask with 0.48 mm^2 area was used. Deposition energy is adjusted by changing the substrate potential, and final deceleration occurs as the ions pass through the mass onto the substrate. During deposition, the substrate is positioned just behind the mask to minimize space-charge-induced spreading of the deposition spot in the final deceleration onto the substrate. To allow sample trans-

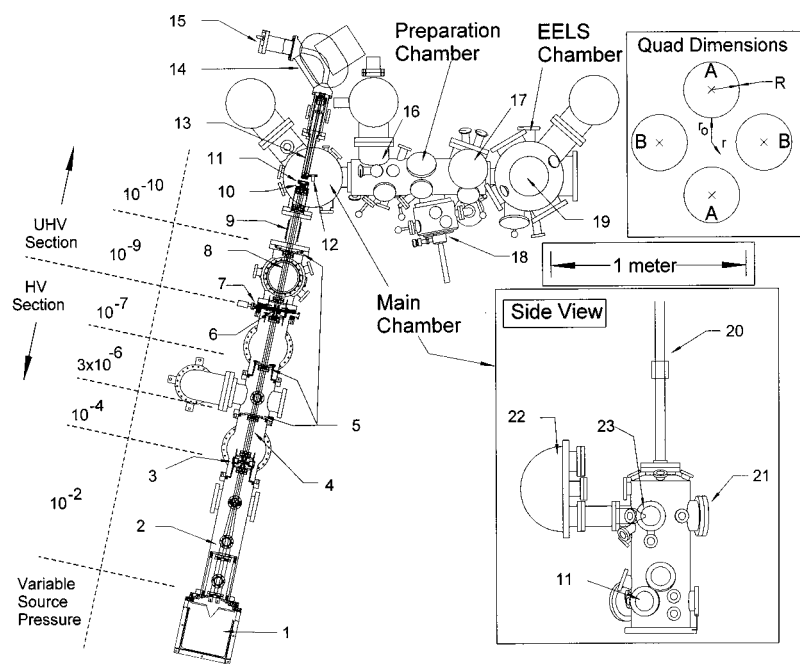


FIG. 1. Utah ion deposition instrument: 1. Ion source chamber, 2. compressing quadrupole trap, 3. einzel lens/differential pumping aperture, 4. low-pass quadrupole, 5. mid-quad differential pumping apertures, 6. lens/differential pumping aperture, 7. UHV-HV isolation valve (built into lens), 8. high-pass quadrupole, 9. isolation bellows, 10. deceleration lenses and exposure mask, 11. deposition station kinematic mount, 12. vertical transporter sample mount, 13. octapole ion guide, 14. magnetic sector mass analyzer, 15. channeltron detector, 16. sample sputter/anneal station, 17. temperature programmed desorption (TPD) station, 18. load lock, 19. EELS chamber and station (manipulator not shown), 20. vertical transporter, 21. scanning tunneling microscopy (STM) station, 22. 150 mm hemispherical energy analyzer, 23. XPS/UPS/Auger station (manipulator not shown).

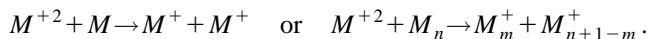
fer, and to accommodate different sample thicknesses, the substrate-mask separation is adjustable.

The ion mass range deposited is determined by the low- and high-pass mass filters in the beamline. To verify the mass selection and to facilitate adjustment of the beamline, we have a 90° deflection, 10.2 cm radius, magnetic mass spectrometer positioned after the deposition station. To use this mass spectrometer, the sample mount is simply removed from the deposition station, allowing the ion beam to pass into a set of collection lenses. The ions are focused into an rf octapole ion guide that transports them ~ 0.4 m to the acceleration lenses of the mass spectrometer. To avoid having to operate the source/beamline at high voltages, the mass spectrometer flight tube is insulated by a glass vacuum break, and floated at the acceleration potential. With the slits currently used, the resolution is $M/\Delta M \approx 100$.

One potential concern for any mass-selecting system is multiply charged ions. For low-mass ions, the resolution of the beamline and final mass spectrometer are sufficient to detect the presence of multiply charged clusters (M_n^{m+}) provided that m/n is nonintegral. For large clusters ($n > 100$), we will not be able to detect multiply charged clusters directly. Fortunately, the cluster sources we use appear not to produce significant numbers of multiply charged cluster ions. This conclusion is based on our gas-phase scattering studies of metal, semimetal, and metal-oxide cluster ions, using laser ablation, laser vaporization, and sputtering sources.^{30,32–36,38,40–47,61} In some of those experiments, a high resolution mass spectrometer⁶² was used, capable of resolving M_n^{m+} (m/n nonintegral) for clusters containing up to several hundred atoms.

The absence of multiply charged cluster ions presumably reflects the kinetics for clusterscan growth/survival in the sources. Cluster size distributions are determined by the balance between various aggregation and dissociation/evaporative cooling processes. Since cation-cation aggregation is energetically unfavorable, forming multiply charged

species is not likely to be efficient. Multiply charged atomic ions may be produced in the sources, but in collisions with other metal atoms or small metal clusters, energetics favor dispersing the charge, for example:



Finally, in the evaporative cooling that occurs in the cluster stabilization process, it is energetically favorable for multiply charged species to lose charge by evaporating ionic species, rather than neutrals.

The surface preparation and analysis capabilities of the instrument are standard, and will not be discussed further. The only feature of interest is the approach taken to working with the small area samples prepared by focused ion beam deposition. We rejected using a conventional manipulator to position the sample in the deposition/analysis stations because we were concerned about positional stability and reproducibility, and because such a manipulator is unsuitable for scanning probe microscopy. Instead, the substrate is mounted on a kinematic stage that can be transferred around in the vacuum system and installed in mounts at each experimental station. The kinematic mount can simultaneously make connections for heating and thermocouples to allow variable temperature work. Positional repeatability and station-to-station positioning accuracy is estimated to be $< 50 \mu\text{m}$ —sufficient to ensure that our small-area analysis tools probe within the deposited spot. In addition to the deposition station there are electron spectroscopy [X-ray photoelectron spectroscopy (XPS)/ultraviolet photoelectron spectroscopy (UPS)/Auger], scanning probe microscopy, sputtering/annealing/vapor deposition, and electron energy loss spectroscopy (EELS) stations. A station for spatially resolved thermal programmed desorption and surface reaction studies is currently being constructed.

Typical operating pressures (mbar) are given at the far left of Fig. 1. The “main,” “preparation,” and “EELS” chambers have base pressures below 10^{-10} mbar, and the

beamline chambers have base pressures $<10^{-7}$ mbar. The high-pass quadrupole chamber serves as the interface between the HV and UHV sections and has a base pressure $<10^{-9}$ mbar. With the exception of the source chamber, the elevated pressures shown under operating conditions almost entirely result from ultrahigh purity argon or helium effusing from the compressing quadrupole chamber.

B. Beamline construction

The beamline chambers are all mounted on individual stands that ride on a bearing/rail system to allow easy movement. The internal parts are mounted on removable bulkheads, such that any part can be serviced by breaking the vacuum system at the appropriate joint, and rolling the chambers apart. Each quad is held in one fixed mount, with at least one other sliding mount. One advantage of guided ion beams is that alignment is straightforward. The end of each quad must be centered on the lens that couples to it; in the present system the lens systems include tapered sleeves that force the quads into alignment as the chambers are rolled together. It is not important, however, that the whole beamline be coaxial, because the quadrupole guides compensate for small angular misalignments.

The beamline, with its large pumps, has noticeable vibration. To avoid coupling this to the analysis chambers, there is an isolation bellows surrounding part of the final quadrupole. To provide vibration isolation from the floor, the analysis chambers are mounted on pneumatic mounts, and the entire section (mass ≈ 1000 kg) can be lifted a few millimeters off its mounting feet. To preserve alignment of the sample spot, the entire deposition station, including lenses, mask, and sample mount; attach to the end of the final quad and remain stationary when the analysis chambers lift.

1. Compressing quadrupole trap

The compressing quad is designed to accept a beam from an ion source, up to 1 cm in diameter. To give a large acceptance aperture, the entrance end of the quad is constructed of 1.9-cm-diam stainless steel rods. Each pair of rods is screwed to a stainless steel holder, and the holders are insulated from each other and from the mounting rings by 5.55-mm-diam ruby balls. The important geometric parameters of the quads are indicated in upper inset of Fig. 1, drawn out-of-scale to allow room for the dimension labels. The rods are mounted such that the ratio $R/r_0 = 1.16$. The entrance section of the quad is 25.4 cm long. In order to deliver a smaller diameter beam, increase residence time, and to improve differential pumping in later sections of the beamline, the exit end of the quadrupole has all radial dimensions scaled down by a factor of 2. The length of this final section is 21.6 cm. Connecting the two straight sections is a 24 cm tapered section. Rod diameter and spacing vary together, such that the R/r_0 ratio is constant. For rigidity, the three sections are welded together. Other than the ruby balls, the quad and its mounts are all stainless steel. This avoids the expense of machining large ceramic insulators, and also avoids insulating surfaces exposed to the ion beam. The quad

is mounted to the supporting bulkheads via rings that are kinematically coupled to the rod holders with ruby ball insulators.

2. Low and high-pass quadrupole ion guides

Apart from the length, the dimensions of these quads are identical to the exit section of the compressing quad. The electrodes are 0.95-cm-diam stainless steel rods, attached to stainless steel holders such that the R/r_0 ratio is 1.16. The low pass quad is 76 cm long, and the high pass quad is 62 cm long. The final two holder/electrode sets of the high pass quad extend into the "main" chamber, and the deposition station is mounted to the quad using ruby ball insulators. This assures that the lenses, mask, and sample are aligned correctly with the beamline, and allows us to pneumatically float the analysis chamber without affecting alignment.

Three of the quad mounts (labeled "5" in Fig. 1) are at vacuum chamber bulkheads, and allow differential pumping. Because the quad passes through these differential walls, the conductance is ~ 20 ℓ/s . In contrast, the lens systems, which also serve as differential pumping apertures, have a conductance of ~ 2 ℓ/s .

Ions are injected into and extracted from the quads by conventional electrostatic lens systems. Between the compressing and low pass quads there is a three element (einzeln) lens, each element having a 6-mm-diam bore, with thicknesses of 6, 4.8, and 6 mm. Between the low- and high-pass quads, a four element lens system is used in order to give room for the UHV isolation valve. The thicknesses of the elements are 6.4, 5.0, 7.7, and 5.8 mm. The first three have 6 mm cylindrical bores, and the final element has a bore that tapers from 5.1 to 4.0 mm. This lens protrudes ~ 1.5 mm into the high pass quad to improve injection efficiency. The third element forms the sealing surface for the isolation valve, and there is a 12.7-mm-diam viton *o*-ring surrounding the lens bore. The 1.5-mm-thick valve slide fits in between the second and third lens elements, and the slide and lens surfaces include beveled protrusions that force the slide against the *o*-ring at the end of its travel. The valve is controlled by a pneumatic, bellows-sealed linear-motion feedthrough that exerts ~ 1 N per square millimeter of sealing surface. This is sufficient to give no detectable pressure rise in the either the HV or analysis sections when the other is vented.

3. Radio frequency source

For this experiment, the quads and final octapole must be driven over a wide frequency range in order to transmit and mass select a wide range of cluster masses. It is also necessary to float the quads at different dc potentials, and to apply small dc difference potentials (see below). For this purpose, we have improved an earlier design for a broadly tunable high-voltage rf oscillator.⁶³ Additional construction details can be found at the "Utah rf generator page" link on the web page at www.chem.utah.edu/chemistry/faculty/anderson/anderson.html. As currently modified, the rf sources can operate at frequencies between 200 kHz and 20 MHz and amplitudes up to 700 V.

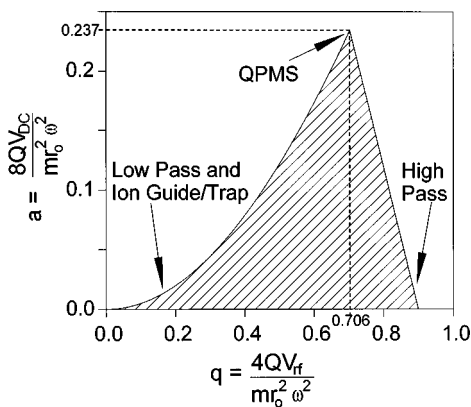


FIG. 2. Stability diagram for transmission of ions through an rf quadrupole [after Dawson (Ref. 64)] “QPMS” denotes the high mass resolution operating conditions used in quadrupole mass spectrometers.

III. DISCUSSION

A. Operating principles

1. Ion motion in rf quadrupoles

The four rods making up each quad are connected together to form two alternating pairs (i.e., A–A and B–B in Fig. 1). The rf of equal amplitude (V_{rf}) but opposite phase is applied to the two pairs. For some applications, we also apply equal but opposite polarity dc difference potentials (V_{dc}) to the two pairs of rods. Finally, to set the average ion energy (the pass energy) in the quad, the entire quad is floated on a common dc potential, V_{float} . Our rf sources provide for all three potentials, and allow V_{rf} and V_{float} to be varied under computer control.

Because of their wide use as mass filters, the theory of ion motion in linear rf quadrupoles has been well established; see the book by Dawson,⁶⁴ for example. More generalized discussions of ion motion in inhomogeneous rf fields are given in reviews by Dehmelt⁶⁵ and Gerlich.²⁸ The quadrupole is a special case because the equations of motion can be solved analytically. The stability of ion trajectories through the quadrupole is normally described in terms of two dimensionless parameters: $a = 8 \times Q \times V_{dc} / (m r_0^2 \omega^2)$ and $q = 4 \times Q \times V_{rf} / (m r_0^2 \omega^2)$, where m is the ion mass, r_0 is the centerline-to-pole distance (Fig. 1), and ω is the rf.

Figure 2 shows a stability diagram for a quadrupole, plotted in terms of the a and q parameters. Only if the ion mass, rf amplitude and frequency, and V_{dc} are such that (a, q) lies within the shaded region of the diagram, will the trajectory be stable and the ion transmitted. For high mass resolution, as in a normal mass filter, the operating conditions are near the apex of the stable region: $q = 0.706$, $a = 0.232$ – 0.237 . This generally requires low rf frequencies and large rf and dc amplitudes.

For use as ion guides, the operating conditions are quite different. As discussed by Gerlich,²⁸ normal guide operating conditions require lower q values (< 0.3 for a quadrupole), typically achieved using higher rf, and/or lower rf amplitudes. The applied dc difference potential V_{dc} is also small or zero ($a \approx 0$). Under these conditions, the amplitude of the rapid oscillations induced by the rf field is small, and is out of phase with the rf driving force. Because the field is inho-

mogeneous, the accelerations toward and away from the quadrupole rods do not quite cancel during each rf cycle, and there is a net force directed toward the quad centerline. The ion motion can be described as large scale motion with superimposed small scale rapid oscillations, due to the rf driving field. The large scale motion is well described by an adiabatic approximation,^{26,28} within which, the ions move as if they are acted on by a *time-independent* effective potential:

$$U_{\text{eff}}(r) = \frac{Q^2 V_{rf}^2}{m \omega^2 r_0^2} \left(\frac{r}{r_0} \right)^2 + Q V_{dc} \cos 2\phi \left(\frac{r}{r_0} \right)^2. \quad (1)$$

The first term is a ponderomotive pseudopotential, equal to the mean kinetic energy of the rapid oscillations, and the second term is the static quadrupolar field due to the applied dc difference potential, if any. Note that the ponderomotive potential always increases with distance from the quad centerline, i.e., it tends to confine the ions. The static potential, on the other hand, attracts the ions toward one pair of rods, and thus tends to destabilize the ion trajectories. Because both parts of the effective potential are quadratic in r , the radial ion motion can be thought of as large-scale harmonic oscillation about the guide/trap centerline, with superimposed small-scale motion due to the applied rf driving field. Stable trapping occurs as long as the large scale oscillations do not carry the ions so close to the rod surfaces that the small-scale motion can cause them to hit the rods. The amplitude of the small scale motion varies with m , ω , r , and V_{rf} , however, a useful rule of thumb is that trapping occurs for ions within the volume defined by $r < \sim 0.8r_0$.

2. Compressing quad

This quad is usually operated with no applied V_{dc} (i.e., $a = 0$) thus a broad range of ion masses are trapped. Nonetheless, it is important to use rf amplitudes and frequencies appropriate for the desired ion mass range. We choose a frequency such that q is ~ 0.2 for V_{rf} of a few hundred volts. Higher rf amplitudes are problematic in this gas-filled quad because they can cause discharges. For typical atomic or molecular ions ($m/Q < 500$), a frequency of a few MHz is suitable, and the amplitude is adjusted to maximize signal for the ion of interest. For much heavier ions, such as large clusters, the operating frequency is decreased accordingly.

Phase space compression requires inert gas collisions to damp the ions' initial kinetic energy. For this purpose, the entire chamber containing the compressing quad is filled to $\sim 10^{-2}$ mbar, giving a mean free path between ion-inert gas collisions of 0.2–1 cm (the collision cross section depends both on energy and ion size). This is short enough to ensure that the ions will collide many times before entering the tapered section of the quad, but long enough that the probability is not too high for collisions while the ions are near their classical turning points in the rf field. The pressure is not found to be critical, and is simply optimized for best focused beam intensity at the desired mass. The purpose of the compressing quad is to introduce damping, and this is best accomplished by a large number of gentle collisions. It is, therefore, desirable to use a buffer gas that is significantly

lighter than the ions in question, so that the center-of-mass collision energies are low. We generally use helium for light ions, and argon for heavy ions.

To increase the number of buffer gas collisions, the entrance section of the compressing quad is operated as an ion trap, thus increasing the residence time. Ions are injected into the compressing quad by an electrostatic lens, the last element of which has a nipple that protrudes a few millimeters into the quadrupole. This element is biased ~ 10 V positive (for cations) relative to the quad centerline (V_{float}) potential, so that the ions are accelerated into the quad. Because the ions lose kinetic energy in collisions, the injection lens potential forms a barrier preventing exit in the source direction. The effective potential provides for radial trapping, and less obviously, also prevents ions from moving through the tapered section of the quad. As the quad tapers (decreasing r_0), the effective potential at any given radius (r) increases like $(1/r_0)^4$ [Eq. (1)]. The corresponding trapping force thus has an axial component opposing transmission through the taper. As ions are continuously injected, ion density builds up in the entrance section until the space charge is large enough to force a steady-state current of ions through the taper into the narrow end of the quad. The tapered section is quite efficient in blocking direct ion transmission. If the potential on the injecting nipple is lowered, thus opening the entrance end of the trap, essentially no ions are transmitted.

Two factors combine to substantially reduce the diameter of the ion beam during passage through the compressing quad. The confining effective potential tightens substantially ($U_{\text{eff}} \propto r_0^{-1}$) as the quad tapers. Simultaneously, buffer gas collisions thermalize the kinetic energy available to drive radial excursions. The final beam diameter is determined by the balance between the applied U_{eff} and the space charge in the narrow section. Since the ions are free to leave the exit end of the compressing quad, the space charge is relatively small there. Our retarding potential measurement suggest that the space charge potential in the final section of the compression quad is < 1 eV. For typical operating rf voltage and frequency ($V_{\text{rf}} = 300$ V, $\omega = 2.5$ MHz), the confining effective potential reaches 1 eV at a radius of 0.56 mm, thus a reasonable upper limit on the beam diameter at the compressing quad exit is ~ 1.1 mm. In addition to the reduction in beam size, the kinetic energy distribution is substantially reduced by buffer gas collisions, and this is important for hyperthermal energy deposition. Estimates of the effect of the compressing quad on beam emittance are given below.

3. Low-pass quad

The operation of a quadrupole guide as a low-pass filter can be understood from Eq. (1) and Fig. 2. The rf ponderomotive pseudopotential holding ions in the guide is inversely proportional to the m/Q ratio, while the dc potential pulling ions toward the negatively biased poles (for cations) is mass independent. It is easy to see that for any given set of V_{rf} , V_{dc} and ω values, there is a cutoff mass beyond which the ponderomotive potential is no longer strong enough to bal-

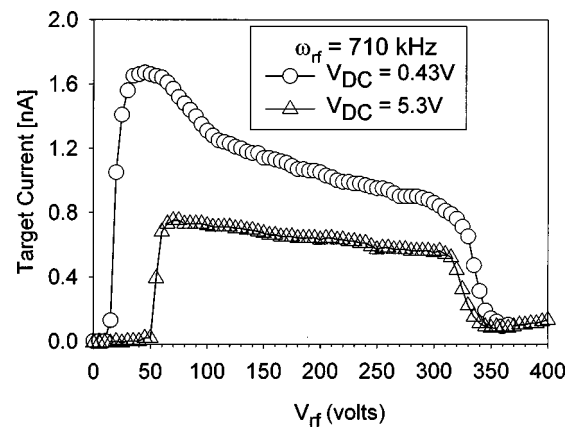


FIG. 3. Transmission of a Xe^+ beam as a function of rf amplitude, showing low- and high-pass behavior.

ance the dc potential. Ions heavier than this cutoff value ($m/Q = V_{\text{rf}}^2 / \omega^2 r_0^2 V_{\text{dc}}$) are lost as the beam propagates through the guide.

The low-pass behavior can clearly be seen in Fig. 3, which gives typical plots of transmission versus V_{rf} , for two different values of the dc difference potential (V_{dc}). The beam for this test was Xe^+ from an electron impact source, with the natural isotope distribution:⁶⁶ ^{128}Xe :1.9%, ¹²⁹ ^{129}Xe :26.4%, ¹³⁰ ^{130}Xe :4.1%, ¹³¹ ^{131}Xe :21.2%, ¹³² ^{132}Xe :26.9%, ¹³⁴ ^{134}Xe :10.4%, ¹³⁶ ^{136}Xe :8.9%. The plots show current focused onto the final deposition target through a 0.48 mm² mask. The quadrupole transmission is quite flat within the range of V_{rf} that leads to stable trajectories, however, there is some change in beam shape that affects downstream focusing. This is the cause of the broad peak near $V_{\text{rf}} = 50$ V in the $V_{\text{dc}} = 0.43$ V curve—focusing through the mask was optimized for low rf and dc. The curve for $V_{\text{dc}} = 5.3$ V was taken without reoptimizing the focusing, and shows the flat V_{rf} dependence of the transmission, albeit with lower focused intensity.

For a small value of V_{dc} (0.43 V), very little rf is required to give stable transmission. As V_{dc} is increased, the rf amplitude needed to stabilize the radial motion also increases (see Fig. 2). For mass filtering, the important point is that the transition from unstable to stable trajectories is quite sharp. Much of the width of the instability–stability transition in Fig. 3 is due to the ~ 5 -amu-wide isotope distribution in Xe^+ . Close examination of the $V_{\text{dc}} = 5.3$ V curve shows a small signal below the onset of stability. This is simply due to a small background from Xe^{++} in this beam.

The resolution of the low-pass quad is affected by several factors. The most important is residence time, which must be long enough to allow ejection of unwanted ion masses, even for ions injected near the axis with low divergence. The residence time can be increased by lowering the ion kinetic energy (pass energy), however, we find that for typical beam currents (5–10 nA) the transmission efficiency begins to drop significantly for pass energies below ~ 30 eV. This appears to result from space charge effects on injection of slow ions into the quads. To increase the residence time, our quads are longer than typical (the length-to-pole-diameter ratios are \sim five to six times those found in typical

quadrupole mass filters). The tradeoff in lengthening the quads is that it becomes more difficult to maintain constant field geometry. If, for example, the average rod-to-center spacing varies over the length, this is equivalent to tuning the mass cutoff value, thus reducing the resolution. From the machining tolerances, we estimate that the average deviation of the rods from their ideal positions is $25\ \mu\text{m}$, and from the equation given above for the cutoff mass, this translates into a contribution to mass broadening of roughly 0.7%. The final factor influencing resolution is space charge distortion of the trapping potentials. Fortunately, the space charge primarily affects the potential near the trap centerline, while the stability is largely determined by dc and rf fields at near the poles. Based both on our observations and on SIMION modeling,⁶⁷ the principle effect is simply to reduce the V_{dc} required to destabilize ions of a given mass.

4. High-pass quad

The effect leading to high-pass operation (i.e., rejection of light ions) can also be seen in Fig. 3. Note that at high rf amplitude, the transmission curves abruptly drop to near zero. As the rf amplitude increases, the force driving the ions also increases. Initially, the principal effect is to increase the ponderomotive pseudopotential confining the ions, thus slightly compressing the beam. When the rf field gets large enough (relative to the ion mass), the adiabatic approximation breaks down, and there is net acceleration from the ion-rf field interaction. Because the accelerations are transverse to the guide axis, they allow the ion to make larger amplitude excursions from the guide centerline, experiencing even larger fields and accelerations. The ion kinetic energy builds rapidly, leading to ejection from the guide.

From the perspective of mass filtering, the important point is that the transition from adiabatic/trapped motion to driven ejection is sharp and mass dependent. High-pass operating conditions correspond to large q , small a , as indicated in Fig. 2. For any given set of operating conditions, the cutoff mass can be estimated from the equations for the high- q border of the stability region,⁶⁸ and is approximately: $m/Q = 4V_{\text{rf}}/\omega^2 r_0^2$. While large q could be generated by simply increasing V_{rf} , it is more practical to drive the high-pass quad at lower frequencies, typically about half the frequency used in the low-pass quad. In addition, we normally apply a dc difference potential (V_{dc}) of a few volts. This potential has little effect on the mass cutoff value, but the small static field helps pull the ions away from the centerline so that trajectory instabilities can build up more quickly. This pull results in a sharper stability/instability transition, and better rejection of unwanted low mass ions. The resolution is affected by the same factors as in the low-pass quad, including the pass energy of ions in the quad, mechanical precision over the length of the quad, and the injection conditions.

IV. PERFORMANCE

To date, we have mostly tested the beamline using rare gas ion beams from an electron impact ion source. As Fig. 3 shows, it is possible to get sharp high- and low-pass cutoffs with confined, high intensity beams. We have also used the

TABLE I. Typical operating potentials of beamline elements. Potentials shown are typical for 35 eV Ar^+ ions on the target.

Element	Typical operating potential (V)
Ion source grid	+25 V
Extraction lens	-100 V
Injection lens	+10 V
Compressing quadrupole (trap)	0 V (reference), $V_{\text{rf}}=300\ \text{V}$, $\omega=2.5\ \text{MHz}$
1st lens	-5 V
2nd lens	-150 V
3rd lens	-25 V
Low-pass quadrupole	-35 V, $V_{\text{rf}}=120\ \text{V}$, $\omega=3.2\ \text{MHz}$
1st lens	-40 V
2nd lens	-150 V
3rd lens	-150 V
4th lens	-40 V
High-pass quadrupole	-45 V, $V_{\text{rf}}=75\ \text{V}$, $\omega=0.8\ \text{MHz}$
Decel lens stack mount	-50 V
1st decel	-15 V
2nd decel	-90 V
3rd decel	-150 V
4th decel	-15 V
5th decel (mask)	-50 V
Sample	-35 V

mass filters to select a particular mass from ions generated in a rare gas mixture in the electron impact source.

Typical operating conditions for deposition using the electron impact ion source are given in Table I. In this source, the ionization volume is partially enclosed by the ion source grid and its potential defines the nominal potential for ion creation. The actual distribution of potential in the ionization volume is determined by electron and ion space charge and the potential applied to the extraction lens. The injection lens is set 10 V positive with respect to the compressing quad to prevent thermalized ions from exiting from the entrance end of the quad. The dc potential of the compressing quad itself is typically set to ground potential, and under thermalizing conditions, the beam kinetic energy in later stages of the beamline is referenced to the compressing quad potential. If the compressing quad is not gas filled, the beam kinetic energy is referenced, instead, to the ion source grid potential. The three element lens between the compressing and low pass quads is operated as a slightly asymmetric einzel lens, and the pass energy in the low pass quad (referenced to the compressing quad) is typically set to between 10 and 50 eV. The four element lens between the low- and high-pass quads was operated, for this example, as a symmetric einzel lens, however all four elements are independently adjustable. We find that transmission from one quad to the next is improved if the pass energy is increased, thus the high pass quad is typically operated 10 V below the low pass quad potential. The deceleration (decel) lens stack is mounted on the end of the high pass quad, and the mount is found to have a slight effect on the beam focusing. It is typically kept near the high-pass quad potential. The decel stack is operated in a mode where the ions are accelerated out of the quad, then decelerated through the mask onto the sample. The nominal deposition energy is simply the difference between the compressing quad potential and the sample potential, 35 eV for the potentials in Table I. When the depo-

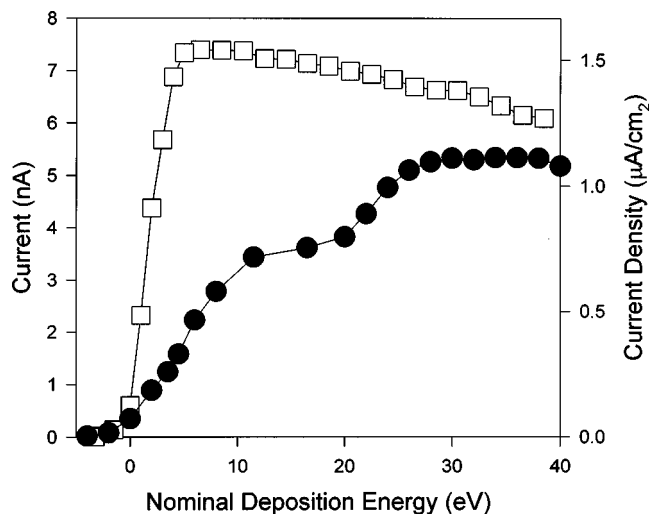


FIG. 4. Transmission of nascent (uncompressed) and phase-space-compressed ion beams through a 0.48 mm^2 pinhole mask onto a substrate, as a function of nominal deposition energy. Filled circles—nascent beam; open squares—compressed beam.

sition energy is changed, the fourth decel and mask potentials must be adjusted to maximize current onto the sample.

From our perspective, the main performance issue is how much the compressing quad improves our ability to focus the beam at hyperthermal energies. Figure 4 gives an example. This experiment was done with an Ar^+ beam generated in the electron impact source. We plot the current delivered to a target through a 0.0048 cm^2 pinhole mask, as a function of the nominal deposition energy. The second vertical axis gives the corresponding average current density, i.e., the measured current divided by the mask area. For the “uncompressed” experiment, the compressing quad was simply used as an ion guide; the chamber around this quad was not filled with helium. For the compressed beam, the compressing quad chamber was filled to $\sim 10^{-2}$ mbar with helium.

Especially for the uncompressed beam, “deposition energy” is rather ill defined because the energy is referenced to the potential of the ionization volume in the source, and this is set by a combination of electrode and ion/electron space charge potentials. The energy of the compressed beam is defined by the potential inside the exit end of the compressing quad, where the final thermalizing collisions occur. This is still uncertain by about 1 eV, due to the space charge potential in the exit section of the quad, but is much better defined than for the nascent beam. For the purposes of these plots, the zero for the deposition energy scale was taken to be the target voltage where about 10% of each beam was collected on the target.

Note that for the uncompressed beam, the target current density rises slowly with energy, and does not saturate until nearly 30 eV. For the compressed beam, the current density rises rapidly, saturating at a nominal energy of ~ 4 eV. The compressed beam can deliver $1 \mu\text{A}/\text{cm}^2$ current density at 3 eV—one tenth the energy required for the same current density with the uncompressed beam. At 3 eV, the current density of the compressed beam is nearly six times greater than that of the uncompressed beam.

The scans of deposition energy were made by fixing all beamline/decel stack potentials relative to the electrical common of the beamline, then varying this common potential relative to that of the target. This has the advantage that beamline transmission is independent of deposition energy, however, the deceleration/focusing conditions between the mask and target vary with energy. For the purposes of demonstrating the high current densities achievable at hyperthermal deposition energies, the voltages on the deceleration/focusing lens stack were optimized at a nominal deposition energy of ~ 2 eV. The decrease in current for the compressed beam at energies above ~ 10 eV simply reflects unoptimized deceleration/focusing conditions. For the uncompressed beam, the current continues to rise with increasing energy because the main factor limiting transmission is the poor beam quality, rather than focusing conditions.

Another useful performance measure is the effect of the compressing quad on beam emittance. Our beamline does not lend itself to direct emittance measurements, however, the emittance can be estimated at several points. The estimates given are for the conditions used to generate the argon beam deposited in Fig. 4. One important quantity is the maximum source emittance that can be accepted by the compressing quad. This is a function of the radius of the injection lens (5 mm) and the maximum injection divergence angle that leads to trapping. We can estimate the maximum injection angle as follows. As discussed by Gerlich²⁸ and summarized above, ions are trapped efficiently as long they remain inside the central volume defined by $r < \sim 0.8r_0$. For the conditions used to generate the compressed argon beam ($\omega = 2.5$ MHz, $V_{rf} = 300$ V), ions with radial velocities less than ~ 6500 m/s will be trapped. For the 25 eV injection energy used, this corresponds to a maximum divergence half angle of ~ 525 mrad. The resulting absolute emittance is $\sim 2600 \pi \text{ mm mrad}$, and the normalized emittance is $\sim 9.6 \times 10^{-2} \pi \text{ mm mrad}$.

The effect of the compressing quad can be estimated at two positions. We can estimate emittance at a plane just *inside* the exit of the compressing quad, prior to extraction. At this point, the ions have thermal kinetic energies, and for the transmitted ions the maximum divergence half angle is 90° . Note, however, that the *transmission-weighted* (i.e., cosine weighted) mean divergence angle is only 32.5° , and 90% of the transmitted ions have divergence angles less than 64° . Using 64° and the estimated radius of the beam (≤ 0.56 mm, see above), we find an absolute emittance of $\leq 630 \pi \text{ mm mrad}$. More importantly, the normalized emittance, assuming thermal velocity, is $\leq 7.4 \times 10^{-4} \pi \text{ mm mrad}$. Relative to the input beam entering the compressing quad, we achieve a reduction in normalized emittance of more than two orders of magnitude.

We can also estimate the emittance at the deposition stage. The estimate is made for a nominal deposition energy of 4 eV—the minimum energy where the beam transmission saturates (Fig. 4). The beam passes through a 0.4 mm radius pinhole that defines the beam size just before deceleration onto the target. To calculate the emittance as the beam hits the target, we need to know how much the beam expands radially between the mask and sample, and how large diver-

gence (impact) angle can be. We have used SIMION⁶⁷ trajectory calculations to estimate the deposition behavior. Because the mask and sample are only separated by 100–200 μm , there is a strong retarding potential gradient ($\sim\text{kV/cm}$). Under these conditions, ions exiting the pinhole along its centerline with divergence angles greater than $\sim 12^\circ$ are deflected from the sample and strike the mask. Ions exiting the pinhole near its periphery must actually be slightly convergent in order to avoid deflection into the mask. The result is that the deposition spot matches the pinhole radius within 10%, i.e., well within the accuracy of the simulation. For the ions that impact the target, the mean impact angle is $\sim 20^\circ$. The resulting absolute emittance at 4 eV on the target is $\sim 140 \pi \text{ mm mrad}$, and the corresponding normalized emittance is $\sim 2 \times 10^{-3} \pi \text{ mm mrad}$. The normalized emittance estimated this way is 2.7 times greater than the estimate for the exit of the cooling quad. This deviation is within the combined uncertainties of the estimates, because neither estimate explicitly includes the effects of space charge on the ion energy or beam divergence. In any case, the estimates both point to a factor of about 100 decrease in normalized emittance, relative to the beam injected into the compressing quad.

This emittance improvement reflects the reduction in beam radius and radial momentum (the radial components of the phase space distribution). For hyperthermal energy deposition, it is equally important that the beam have a narrow kinetic energy distribution, otherwise the deposition energy is ill defined and transmission efficiency is poor. For the high pressure sources used for cluster generation, extraction conditions that optimize ion intensity often lead to broad (>30 eV) beam energy spreads because collisions occur during extraction. The energy spread of the Ar^+ beam used for this example was measured to be ~ 20 eV by retarding potential analysis. Our goal is deposition at energies of a few electron volts, thus we require energy spreads less than ~ 1 eV. The compressing quad solves this problem by thermalizing the injected ions, and allows the source to be operated for maximum intensity, without regard for energy spread. Our beam energy spreads, measured by retarding potential analysis are typically <1 eV full width at half maximum (FWHM).

Even with the small diameter, low current ion source used in these tests, the deliverable hyperthermal energy current density is already quite substantial, corresponding to monolayer/minute exposure rates. The compressing quad is capable of accepting an ion beam with substantially higher current and beam size than our electron-impact source, and we believe that the brightness of the beamline should scale well with source current. We do not have the means to measure focal spot sizes smaller than a few hundred microns, and thus are unable to study the effects of phase space compression on focusability at higher beam energies. Still, it is almost certain that the minimum spot size would continue to decrease, and current density increase as the energy is raised. Phase-space compression might therefore be valuable in generation of tightly focused beams at high energies.

ACKNOWLEDGMENTS

Development of the instrument is supported by the Air Force Office of Scientific Research under Grant No. F49620-96-1-0119. We are grateful to Eastman Kodak Inc (Gustav Apai) for donation of a VG ESCALAB Mark II that we have used for part of the vacuum/pumping system. Dennis Romney and the chemistry machine shop staff produced the beamline components and provided helpful design suggestions.

- ¹D. Marton, in *Low Energy Ion-Surface Interactions*, edited by J. W. Rabalais (Wiley, New York, 1994), p. 481ff.
- ²J. E. Bower and M. F. Jarrold, *J. Chem. Phys.* **97**, 8312 (1992).
- ³U. Heiz, R. Sherwood, D. M. Cox, A. Kaldor, and J. T. Yates, *NATO ASI Ser., Ser. C* **465**, 37 (1995).
- ⁴H. V. Roy, P. Fayet, F. Patthey, W. D. Schneider, B. Delley, and C. Massobrio, *Phys. Rev. B* **49**, 5611 (1994).
- ⁵H. V. Roy, F. Patthey, P. Fayet, W. D. Schneider, and B. Delley, *Surf. Rev. Lett.* **3**, 943 (1996).
- ⁶F. Vanolli, U. Heiz, and W.-D. Schneider, *Chem. Phys. Lett.* **277**, 527 (1997).
- ⁷P. Fayet, W. Eberhardt, D. M. Cox, Z. Fu, R. Sherwood, D. Sondericker, and A. Kaldor, in *Synchrotron Radiat.: Sel. Exp. Condensed Matter Physics*, edited by W. Czaja (Birkhaeuser, Basel, Switzerland, 1990), p. 83.
- ⁸H. V. Roy, J. Boschung, P. Fayet, F. Patthey, and W. D. Schneider, *Z. Phys. D: At., Mol. Clusters* **26**, 252 (1993).
- ⁹P. Fayet, F. Granzer, G. Hegebart, E. Moisar, and B. Pischel, *Phys. Rev. Lett.* **55**, 3002 (1985).
- ¹⁰W. Eberhardt, P. Fayet, D. M. Cox, Z. Fu, A. Kaldor, R. Sherwood, and D. Sondericker, *Phys. Rev. Lett.* **64**, 780 (1990).
- ¹¹W. Eberhardt, P. Fayet, D. Cox, Z. Fu, A. Kaldor, R. Sherwood, and D. Sondericker, *Phys. Scr.* **41**, 892 (1990).
- ¹²W. Eberhardt, D. M. Cox, Z. Fu, A. Kaldor, R. Sherwood, and D. Sondericker, *Phys. Rev. Lett.* **64**, 780 (1990).
- ¹³S. J. Carroll, K. Seeger, and R. E. Palmer, *Appl. Phys. Lett.* **72**, 305 (1998).
- ¹⁴L. C. Chao and R. P. Andres, *J. Colloid Interface Sci.* **165**, 290 (1994).
- ¹⁵E. Choi and R. P. Andres, *NATO ASI Ser., Ser. B* **158 Ph.** 61 (1987).
- ¹⁶Y. Z. Li, R. Reifengerger, E. Choi, and R. P. Andres, *Surf. Sci.* **250**, 1 (1991).
- ¹⁷S. T. Lin and R. P. Andres, *Mater. Res. Soc. Symp. Proc.* **317**, 149 (1994).
- ¹⁸W. Mahoney, D. M. Schaefer, A. Patil, R. P. Andres, and R. Reifengerger, *Surf. Sci.* **316**, 383 (1994).
- ¹⁹D. M. Schaefer, A. Patil, R. P. Andres, and R. Reifengerger, *Phys. Rev. B: Condens. Matter* **51**, 5322 (1995).
- ²⁰D. M. Schaefer, R. Reifengerger, A. Patil, and R. P. Andres, *Appl. Phys. Lett.* **66**, 1012 (1995).
- ²¹G. Fuchs, P. Melinon, Y. Yan, B. Cabaud, A. Hoareau, M. Treilleux, and V. Paillard, *Z. Phys. D: At., Mol. Clusters* **26**, 249 (1993).
- ²²P. Melinon, B. Prevel, V. Dupuis, A. Perez, B. Champagnon, Y. Guyot, M. Boudeulle, M. Pellarin, J. Lerme, and M. Broyer, *Z. Phys. D: At., Mol. Clusters* **40**, 554 (1997).
- ²³Y. Guyot, B. Champagnon, M. Boudeulle, P. Melinon, B. Prevel, V. Dupuis, and A. Perez, *Thin Solid Films* **297**, 188 (1997).
- ²⁴Y. Kuk, M. F. Jarrold, P. J. Silverman, J. E. Bower, and W. L. Brown, *Phys. Rev. B* **39**, 11168 (1989).
- ²⁵K. Bromann, C. Felix, H. Brune, W. Harbich, R. Monot, J. Buttet, and K. Kern, *Science* **274**, 956 (1996).
- ²⁶L. D. Landau and E. M. Lifshitz, *Mechanics* (Pergamon, Oxford, 1960).
- ²⁷R. Keller, in *The Physics and Technology of Ion Sources*, edited by I. G. Brown (Wiley, New York, 1989), p. 23.
- ²⁸D. Gerlich, *Adv. Chem. Phys.* **82**, 1 (1992).
- ²⁹E. Teloy and D. Gerlich, *Chem. Phys.* **4**, 417 (1974).
- ³⁰L. Hanley, S. A. Ruatta, and S. L. Anderson, *J. Chem. Phys.* **87**, 260 (1987).
- ³¹L. Hanley and S. L. Anderson, *J. Phys. Chem.* **91**, 5161 (1987).
- ³²L. Hanley and S. L. Anderson, *J. Chem. Phys.* **89**, 2848 (1988).
- ³³L. Hanley, J. L. Whitten, and S. L. Anderson, *J. Phys. Chem.* **92**, 5803 (1988).
- ³⁴P. Hintz, S. A. Ruatta, and S. L. Anderson, *J. Chem. Phys.* **92**, 292 (1990).

- ³⁵P. A. Hintz, M. B. Sowa, S. A. Ruatta, and S. L. Anderson, *J. Chem. Phys.* **94**, 6446 (1991).
- ³⁶P. A. Hintz, M. B. Sowa, and S. L. Anderson, *Chem. Phys. Lett.* **177**, 146 (1991).
- ³⁷D. Peiris, A. Lapicki, S. L. Anderson, R. Napora, D. Linder, and M. Page, *J. Phys. Chem. A* **101**, 9935 (1997).
- ³⁸S. A. Ruatta, L. Hanley, and S. L. Anderson, *Chem. Phys. Lett.* **137**, 5 (1987).
- ³⁹S. A. Ruatta, L. Hanley, and S. L. Anderson, *J. Chem. Phys.* **89**, 273 (1988).
- ⁴⁰S. A. Ruatta, L. Hanley, and S. L. Anderson, *J. Chem. Phys.* **91**, 226 (1989).
- ⁴¹S. A. Ruatta and S. L. Anderson, *J. Chem. Phys.* **94**, 2833 (1991).
- ⁴²J. Smolanoff, A. Lapicki, N. Kline, and S. L. Anderson, *J. Phys. Chem.* **99**, 16276 (1995).
- ⁴³M. B. Sowa, P. A. Hintz, and S. L. Anderson, *J. Chem. Phys.* **95**, 4719 (1991).
- ⁴⁴M. B. Sowa and S. L. Anderson, *J. Chem. Phys.* **97**, 8164 (1992).
- ⁴⁵M. B. Sowa-Resat, J. N. Smolanoff, A. Lapicki, and S. L. Anderson, *J. Chem. Phys.* **106**, 9511 (1997).
- ⁴⁶M. Sowa-Resat, P. A. Hintz, and S. L. Anderson, *J. Phys. Chem.* **99**, 10736 (1995).
- ⁴⁷M. B. Sowa-Resat, J. N. Smolanoff, I. B. Goldman, and S. L. Anderson, *J. Chem. Phys.* **100**, 8784 (1994).
- ⁴⁸W. Paul, B. Lücke, S. Schlemmer, and D. Gerlich, *Int. J. Mass Spectrom. Ion Processes* **150**, 373 (1995).
- ⁴⁹W. Paul, S. Schlemmer, B. Lücke, and D. Gerlich, *Chem. Phys.* **209**, 265 (1996).
- ⁵⁰T. Leisner, C. Rosche, S. Wolf, F. Granzer, and L. Woeste, *Surf. Rev. Lett.* **3**, 1105 (1996).
- ⁵¹J. H. Freeman, W. Temple, D. Beanland, and G. A. Gard, *Nucl. Instrum. Methods* **135**, 1 (1976).
- ⁵²H. Hofsäass, H. Binder, T. Klumpp, and E. Recknagel, *Diamond Relat. Mater.* **3**, 137 (1994).
- ⁵³A. H. Al-Bayati, D. Marton, S. S. Todorov, K. J. Boyd, D. G. Armour, J. S. Gordon, G. Duller, and J. W. Rabalais, *Rev. Sci. Instrum.* **65**, 2680 (1994).
- ⁵⁴J. H. Freeman, in *International Conference on Applications of Ion Beams to Semiconductor Technology*, Gap, France, 1967 (unpublished).
- ⁵⁵J. S. Colligon, W. A. Grant, J. S. Williams, and R. P. Lawson, *Applications of Ion Beams to Materials 1975*, Proceedings of the Institute of Physics Conference Series, 28, 357.
- ⁵⁶R. A. Zuhr, B. R. Appleton, N. Herbots, B. C. Larson, T. S. Noggle, and S. J. Pennycook, *J. Vac. Sci. Technol. A* **5**, 2135 (1987).
- ⁵⁷F. X. Qin, X. Wang, Z. Liu, Z. Yao, Z. Ren, L. Lin, S. Su, W. Jiang, and W. M. Lau, *Rev. Sci. Instrum.* **62**, 2322 (1991).
- ⁵⁸H. Yamada, H. Inokawa, and T. Takagi, *Nucl. Instrum. Methods Phys. Res. B* **6**, 439 (1985).
- ⁵⁹T. Ohnishi, Y. Yoshida, Y. Hirofuji, and H. Iwasaki, *Nucl. Instrum. Methods Phys. Res. B* **37/38**, 850 (1989).
- ⁶⁰S. Tamura, M. Hyouzho, K. Yokota, and S. Katayama, *Nucl. Instrum. Methods Phys. Res. B* **37/38**, 862 (1989).
- ⁶¹L. Hanley and S. L. Anderson, *Chem. Phys. Lett.* **122**, 410 (1985).
- ⁶²Y. Basir, J. F. Christian, Z. Wan, and S. L. Anderson, *Int. J. Mass Spectrom. Ion Processes* **171**, 159 (1997).
- ⁶³R. M. Jones, D. Gerlich, and S. L. Anderson, *Rev. Sci. Instrum.* **68**, 3357 (1997).
- ⁶⁴P. H. Dawson, *Quadrupole Mass Spectrometry* (Elsevier Scientific, Amsterdam, 1976).
- ⁶⁵H. G. Dehmelt, in *Advances in Atomic and Molecular Physics*, Vol. 3, edited by D. R. Bates (Academic, New York, 1967).
- ⁶⁶*CRC Handbook of Chemistry and Physics*, edited by R. C. Weast, M. Astle, and W. H. Beyer (Chemical Rubber, Boca Raton, FL, 1985).
- ⁶⁷D. A. Dahl, *SIMION*, 6 ed. (Idaho National Engineering Laboratory, Idaho Falls, 1995).
- ⁶⁸P. H. Dawson, *Quadrupole Mass Spectrometry* (Elsevier Scientific, Amsterdam, 1976).